A partially interpenetrated metal–organic framework for selective hysteretic sorption of carbon dioxide

Sihai Yang[1]*, Xiang Lin[1], William Lewis[1], Mikhail Suyetin[1], Elena Bichoutskaia[1], Julia E. Parker[2], Chiu C. Tang[2], David R. Allan[2], Pierre J. Rizkallah[3], Peter Hubberstey[1], Neil R. Champness[1], K. Mark Thomas[4], Alexander J. Blake[1] and Martin Schröder[1]*

The selective capture of carbon dioxide in porous materials has potential for the storage and purification of fuel and flue gases. However, adsorption capacities under dynamic conditions are often insufficient for practical applications, and strategies to enhance CO_2–host selectivity are required. The unique partially interpenetrated metal–organic framework NOTT-202 represents a new class of dynamic material that undergoes pronounced framework phase transition on desolvation. We report temperature-dependent adsorption/desorption hysteresis in desolvated NOTT-202a that responds selectively to CO_2. The CO_2 isotherm shows three steps in the adsorption profile at 195 K, and stepwise filling of pores generated within the observed partially interpenetrated structure has been modelled by grand canonical Monte Carlo simulations. Adsorption of N_2, CH_4, O_2, Ar and H_2 exhibits reversible isotherms without hysteresis under the same conditions, and this allows capture of gases at high pressure, but selectively leaves CO_2 trapped in the nanopores at low pressure.

T he construction of microporous metal–organic framework (MOF) materials has attracted much attention owing to their potentially high internal surface areas and gas storage capabilities, especially for carbon dioxide (CO_2) capture[1–5]. Adsorption capacities of CO_2 at ambient temperature in these porous framework materials can be significantly higher than those of commercial materials[6–8]. However, the storage capacities in MOF materials are reduced markedly when the system is exposed to gaseous mixtures under dynamic conditions[9]. Thus, increasing the selectivity for CO_2 in the presence of gaseous mixtures represents a major challenge if these systems are to find practical applications under dynamic conditions. Several strategies have been explored to enhance the interaction between CO_2 and host frameworks to improve their capture abilities[10–14]; however, none of the proposed strategies is ultimately effective owing to drop-off of selectivity with increased loadings[11,12] or limited total storage capacities of systems where selectivity relies on narrow pores within the MOF (ref. 13).

A particularly attractive approach to improve the selectivity of MOFs to capture CO_2 is to exploit CO_2-triggered framework phase transformations within a flexible host framework material. Given the significant quadrupole moment of CO_2 (-1.4×10^{-39} C m^2), it is possible that molecules such as CO_2 can impart network flexibility and thus induce phase transitions in the framework structure through its quadrupole[15–24]. Interpenetration is commonly thought of as being counter-productive in preparing porous MOFs as the interpenetration is often unpredictable and tends to reduce the porosity of the resultant material. Herein, we report a new type of MOF that exhibits interpenetration of two frameworks but where one of the frameworks is only partially occupied. This is a unique
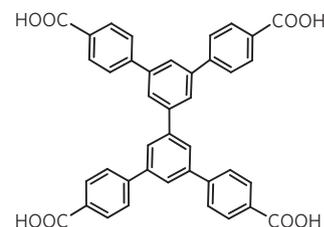
Figure 1 | Chemical structure of H_4L. This ligand has approximate dimensions of 14.6 × 14.7 Å.

example of such a structural arrangement and can be considered as a new class of porous material. Importantly, the structure exhibits unusual materials properties, showing selective hysteretic CO_2 adsorption/desorption as a direct result of the observed partially interpenetrated structure, which has been further modelled by grand canonical Monte Carlo simulations.

Solvothermal reaction of H_4L (biphenyl-3,3′,5,5′-tetra-(phenyl-4-carboxylic acid)) (Fig. 1) with $In(NO_3)_3$ in an acidic (HNO_3) mixture of CH_3CN/DMF(dimethylformamide) ($v/v = 1:2$) at 90 °C affords the solvated framework complex $(Me_2NH_2)_{1.75}[In(L)]_{1.75}(DMF)_{12}(H_2O)_{10}$ (NOTT-202). The counter-cation $Me_2NH_2^+$ is generated by *in situ* decomposition of the DMF solvent during the reaction. The single-crystal X-ray structure of NOTT-202 shows a three-dimensional (4,4)-connected coordination framework constructed from mononuclear $[In(O_2CR)_4]$ nodes each linked to four others by four tetracarboxylate ligands L^{4-} (Fig. 2a,b). The framework structure is interpenetrated and

[1]School of Chemistry, University of Nottingham, University Park, Nottingham NG7 2RD, UK, [2]Diamond Light Source, Harwell Science and Innovation Campus, Didcot OX11 0DE, UK, [3]STFC Daresbury Laboratory, Warrington WA4 4AD, UK, [4]Northern Carbon Research Laboratories, Sir Joseph Swan Institute for Energy Research and School of Chemical Engineering and Advanced Materials, University of Newcastle upon Tyne, Newcastle upon Tyne NE1 7RU, UK. *e-mail: Sihai.Yang@nottingham.ac.uk; M.Schroder@nottingham.ac.uk.
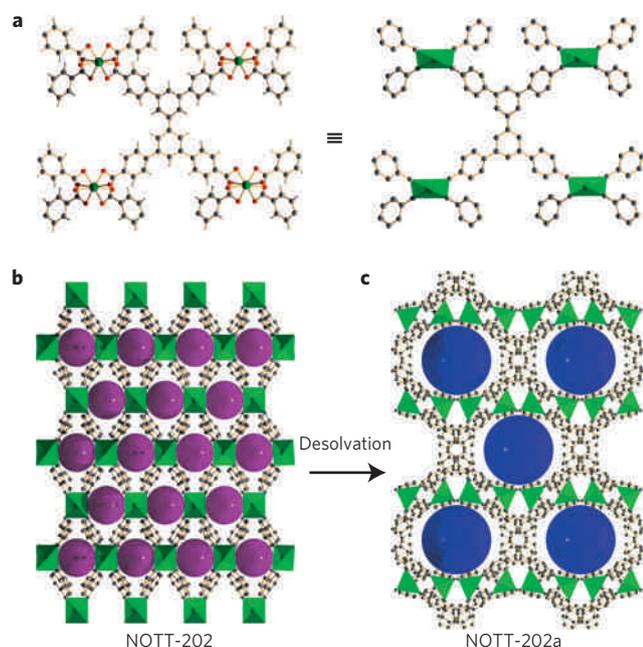
Figure 2 | X-ray crystal structures of NOTT-202 and NOTT-202a. a, View of the coordination environment at the $[In(O_2CR)_4]$ nodes and ligands L^{4-}. The $[In(O_2CR)_4]$ nodes are represented by green tetrahedra. **b,c**, Schematics of pore framework structure for NOTT-202 (**b**) and NOTT-202a (**c**). (Indium: green; oxygen: red; carbon: grey; hydrogen: grey. $[In(O_2CR)_4]$ node: green tetrahedra; cavity in NOTT-202: purple sphere; cavity in NOTT-202a: blue sphere.) In NOTT-202, a rhombic-shaped channel running along the crystallographic b axis is formed by the alternate interweaving of the two independent networks. The approximate diameter of the channel window taking into account the van der Waals radii of the surface atoms is 5.0×5.0 Å (purple sphere) and is defined by the geometry of the $[In(O_2CR)_4]$ moiety and the span of the di-p-carboxylic phenyl moiety on each terminus of the bridging ligand. In contrast, viewed along the same direction, formation of NOTT-202a involves rearrangement of the interweaving of the two independent networks to afford a spherical channel with much wider channel windows of 9.0×9.0 Å (blue sphere).

consists of two crystallographically independent nets (A and B). In net A, the In(III) centre In1 occupies a $4a$ site (symmetry $222 = D_2$) of space group $F222$. Each In(III) is 8-coordinate through binding to O centres from four chelating carboxylate groups [In–O = 2.209(5) and 2.355(7) Å] to form a tetrahedral 4-connected node. Each ligand binds to four separate In(III) centres and acts as a tetrahedral 4-connected node giving net A an overall binodal diamondoid topology (Supplementary Fig. S2). The total void volume available to guest molecules in NOTT-202, taking into account the counter-cations, was estimated by PLATON/SOLV calculations (ref. 25) to be 60%.

In net B, the In(III) centre In2 resides on the lower symmetry $8i$ site (symmetry $2 = C_2$) in space group $F222$ and exhibits an 8-coordinate geometry similar to that in net A, with In–O distances ranging from 2.208(13) to 2.341(17) Å. In contrast to net A, net B is composed of two disordered equally occupied nets (B_1 and B_2) that are interwoven into each other (Supplementary Fig. S5). Nets B_1 and B_2 have the same diamondoid topology and (4,4) coordination geometry as net A, but the crystallographic occupancy of each network B_1 and B_2 is limited to a maximum of 0.5 by the overlapping of these two disordered, symmetry-related components. However, refinement with the occupancy of net B fixed at 0.5 results in an equivalent displacement parameter (U_{eq}) for atom In2 that is significantly larger than that of In1, indicating that the crystallographic occupancy of net B cannot reach the

maximum value of 0.5. The occupancy of net B was, therefore, refined giving a value of 0.374(3) at convergence. Single-crystal X-ray diffraction data collected on four other crystals from four different batches of synthesis and using four different radiation sources gave precisely the same structural model with similar occupancy parameters for net B of 0.394(3), 0.390(4), 0.372(3) or 0.369(3) (Supplementary Table S1). Thus, the overall structure can be viewed as a partially interpenetrated framework with the ratio of two nets, A and B, of 1:0.75 by considering the symmetry of each In(III) site in the orthorhombic space group $F222$. This is a distinct and new form of framework interpenetration/catenation and as such represents a new class of porous material[26–30].

Interpenetration in MOF structures can be successfully controlled by variation of temperature and concentration in synthesis or by using liquid-phase epitaxy on an organic template[31–33]. The formation of non-integral interpenetration observed in NOTT-202 with a dominant net (A) and a secondary net (B) with occupancy 0.75 may provide key insights into the mechanism of formation of interpenetrated structures, and also requires explanation. Net B_1 or net B_2 can be present in any region of the crystal. The only allowed connections are of type $B_1 \rightarrow B_1$ or $B_2 \rightarrow B_2$, as $B_1 \rightarrow B_2$ or $B_2 \rightarrow B_1$ linkages are forbidden because they lead to overlapping of ligand components and steric clashes (Supplementary Fig. S5b). Given the symmetry adopted by net A, a unique fully occupied net B would have to occupy a single position rather than two symmetry-related ones and the resultant flattening, even if geometrically feasible, would mean that it would not fit inside net A. Therefore, having a fully occupied net B within this structural entanglement is not possible. Therefore, maximum interpenetration through net A requires the presence of both nets B_1 and B_2. There cannot be a 0.5 occupancy for each of net B_1 and net B_2 because that would require the spaces between the B_1 and B_2 nets to be filled with metal–ligand connections; these spaces have to be empty because net B_1 cannot connect to net B_2 owing to the resultant steric clashes between ligands on different nets (Supplementary Fig. S5b). The occupancy of 0.75 for net B can thus be traced to the presence of alternative blocks of B_1 or B_2 nets with defects between them. We suggest that nets B_1 and B_2 are initiated at random within net A, leading to these having the same occupancy of 0.375, giving a total occupancy of 0.75 for the combined net B (Fig. 3).

Interestingly, a new phase (NOTT-214; $[Me_2NH_2][In(L)](H_2O)$) can be isolated from the high-temperature synthesis of NOTT-202 (Supplementary Table S3). The single-crystal structure determination confirms that NOTT-214 has the same topology as NOTT-202 but is fourfold interpenetrated with a significantly reduced porosity (Supplementary Fig. S8) of less than 4% pore volume based on PLATON/SOLV (ref. 25) calculations. Thus, NOTT-214 can be viewed as a non-porous analogue of NOTT-202. Comparison of these two crystal structures indicates that the complex partial interpenetration and disordered net fragmentation in NOTT-202 result in a potentially more accessible pore volume, with a significantly higher internal surface area than conventional interpenetrated structures[26–30,34]. Indeed, its corresponding desolvated material $[Me_2NH_2]_{1.75}[In(L)]_{1.75}$ (NOTT-202a) exhibits the highest Brunauer–Emmett–Teller (BET) surface area and micropore volume for any In(III)-based[35] MOF.

The single-crystal structure determination of the desolvated complex NOTT-202a reveals a significant structural phase transition on guest removal from NOTT-202 (Fig. 2c). The metal–ligand coordination and framework topology (4,4-connected) remain the same; however, the crystal structure of NOTT-202a is monoclinic with space group $C2/c$, and the unit cell volume expands by $\sim$11%. The In(III) centre in NOTT-202a is 7-coordinate through binding to oxygen atoms from four carboxylate groups [In–O = 2.109(2) – 2.330(2) Å], leaving one oxygen atom O4 of a
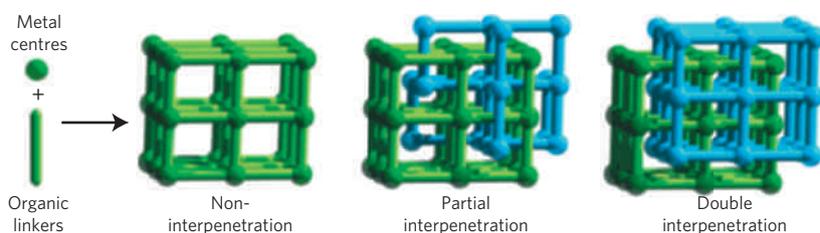
Figure 3 | Representation of self-assembly and interpenetration in three-dimensional MOF materials. The unique partial interpenetration of NOTT-202 composed of one dominant network and one secondary partially formed network. The dominant network is in green and the secondary network is in cyan.
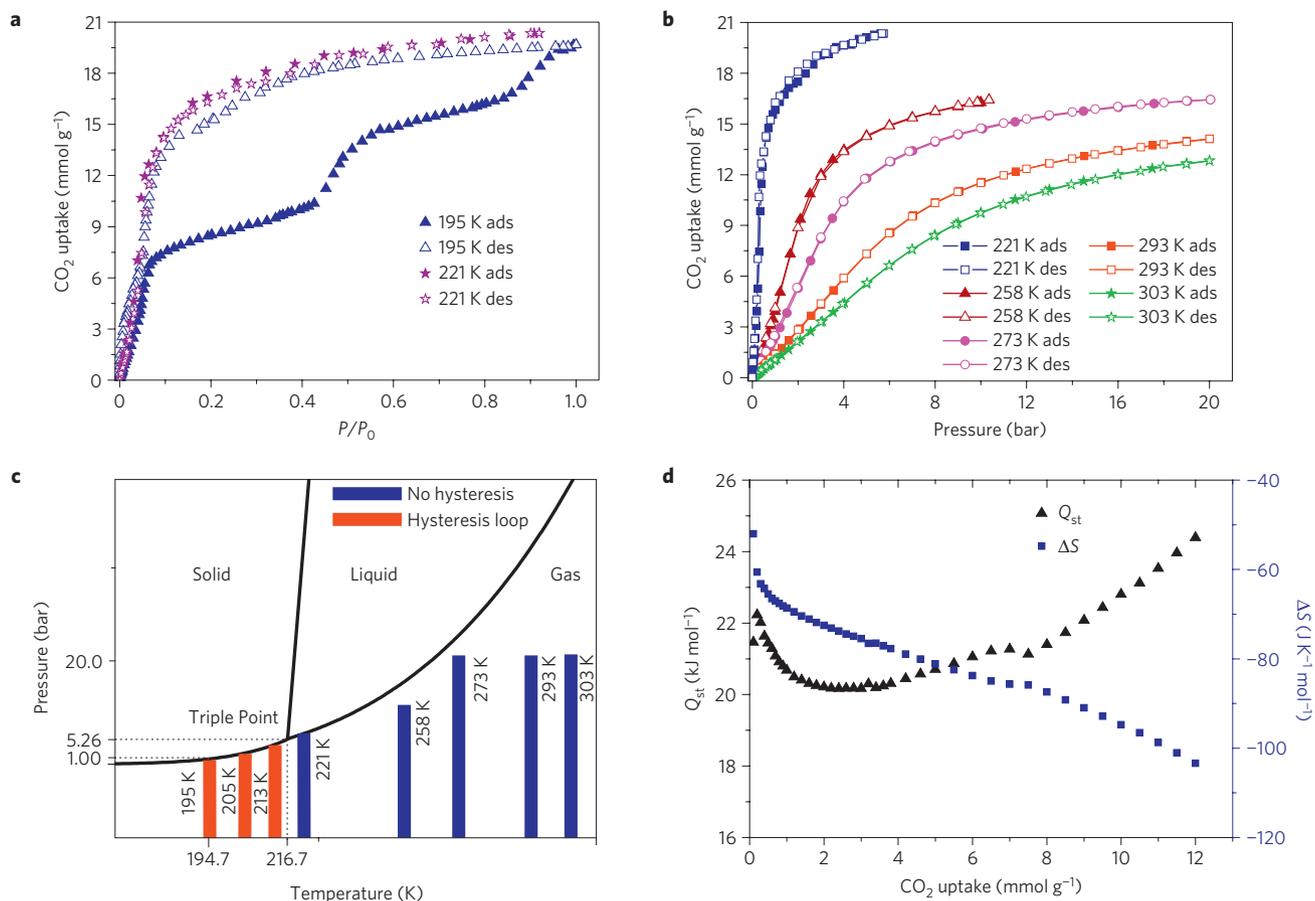
Figure 4 | CO$_2$ sorption isotherms and variation of thermodynamic parameters Q_{st} and ΔS as a function of CO$_2$ uptake in NOTT-202a. a, CO$_2$ sorption isotherms at 195 and 221 K. **b**, CO$_2$ sorption isotherms at various temperatures between 221 and 303 K. **c**, CO$_2$ phase diagram with CO$_2$ sorption isotherms for NOTT-202a at different temperatures. **d**, Thermodynamic parameters Q_{st} and ΔS. The isosteric adsorption enthalpies (Q_{st}) and entropies (ΔS) for CO$_2$ adsorption for various amounts adsorbed were calculated using the van't Hoff isochore for isotherms over the temperature range 195–303 K. At low CO$_2$ uptakes (<7 mmol g^{-1}) the isotherms are consistent with the van't Hoff isochore over the complete temperature range. At higher CO$_2$ uptakes (>7 mmol g^{-1}), Q_{st} and ΔS were calculated from the non-hysteretic isotherms (221–303 K) above the triple point. Both these temperature ranges are large for linear van't Hoff isochore plots. Overall, ΔS decreases continuously with increasing surface coverage for the whole range.

carboxylate donor placed at a distance of 2.774(3) Å from the In(III) centre (Supplementary Fig. S6). Interestingly, the [Me$_2$NH$_2$]$^+$ counter-cations, previously disordered in NOTT-202, are now well located within the pore of NOTT-202a, with NH$_2^+$ groups forming hydrogen bonds with O4, N···O4 = 2.984(4) Å, N–H···O4 = 153° (Supplementary Fig. S6). The free volume fraction/voids in NOTT-202a were estimated by PLATON/SOLV (ref. 25) calculations to be 70%, higher than that of NOTT-202. Thus, importantly, on guest removal, the resultant framework shows larger pores with a more accessible pore volume. Single-crystal data of NOTT-202a collected at various temperatures between 120 and 260 K show that the unit cell volume expands with increasing temperature, confirming a degree of flexibility in the framework (Supplementary Table S2).

The acetone-exchanged sample of NOTT-202 (Me$_2$NH$_2$)$_{1.75}$ [In(L)]$_{1.75}$ · n(Me$_2$CO) was treated at 100 °C and 10^{-7} mm Hg for 1 day to give a fully desolvated sample of NOTT-202a. From N$_2$ adsorption data, the BET surface area was calculated to be 2,220 m^2 g^{-1} with a total micropore volume of 0.953 cm^3 g^{-1}. Gravimetric H$_2$ adsorption isotherms at 77 K show good reversibility and an absence of hysteresis, and give a total storage capacity of 1.52 wt% at 1.0 bar and 4.35 wt% at 20 bar (Supplementary Fig. S24).

In contrast to the highly reversible type-I isotherms observed for N$_2$, Ar and H$_2$ uptakes, the adsorption isotherm for CO$_2$ at 195 K exhibits three distinct steps at $P/P_0 = 0.07$, 0.52 and 0.95 with uptake capacities of ~7, 14 and 20 mmol g^{-1}, respectively (Fig. 4a). The maximum CO$_2$ storage capacity in NOTT-202a (20 mmol g^{-1}
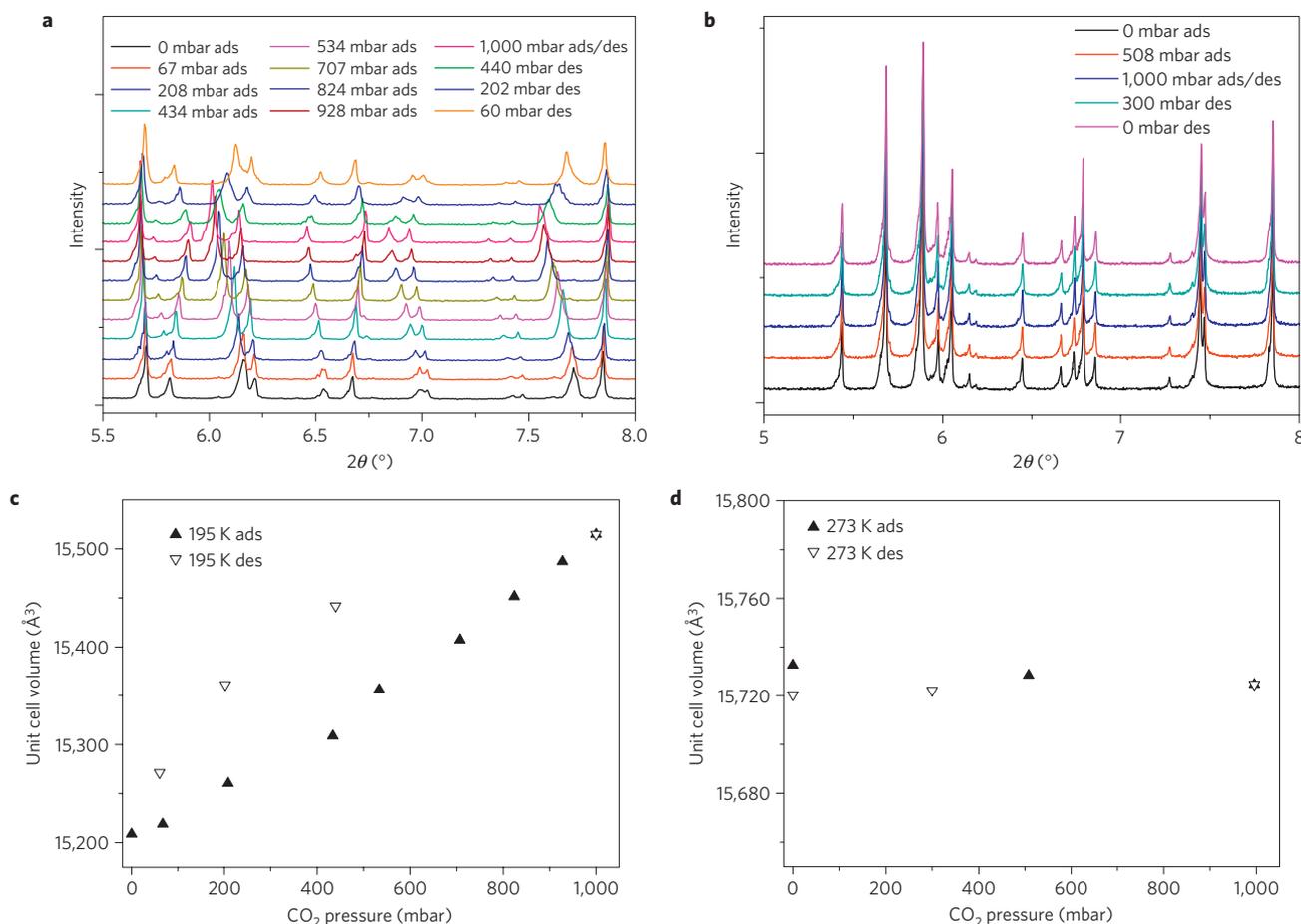
Figure 5 | *In situ* synchrotron X-ray powder diffraction patterns and Le Bail refinement results for NOTT-202a. (Data collected at Diamond Light Source, Beamline I11, $\lambda = 0.82695$ Å.) A powder sample of NOTT-202a was loaded into a capillary tube attached to the sample cell, which was evacuated under vacuum to obtain the fully degassed sample. **a**, Powder X-ray diffraction patterns at different CO_2 adsorption/desorption loadings at 195 K (the powder patterns of NOTT-202a were recorded at 195 K at 0, 67, 208, 434, 534, 707, 824, 928 and 1,000 mbar of CO_2 adsorption loadings and at 440, 202 and 60 mbar of CO_2 desorption loadings). **b**, Powder X-ray diffraction patterns at different CO_2 adsorption/desorption loadings at 273 K. **c,d**, Results of Le Bail fitting of the unit cell volume with different CO_2 loadings at 195 K (**c**) and at 273 K (**d**) at CO_2 loading of 1–2.44 mmol g^{-1}. The Le Bail refinement of the complete set of patterns at 195 K confirms that the space group symmetry remains the same throughout but that the unit cell volume is continually expanding with increasing CO_2 loading. However, on desorption the unit cell volumes do not track the adsorption branch: a hysteresis loop for the unit cell volume is observed between adsorption and desorption of CO_2 in NOTT-202a, consistent with the observed hysteretic release of CO_2 in the isotherms. The Le Bail refinements of the powder patterns at 273 K confirm that the unit cell remains the same at all measured CO_2 loadings with no hysteresis loop observed, consistent with good reversibility of CO_2 uptake and release at 273 K.

at 195 K and 1.0 bar) is higher than previously reported values for In(III)-based[35] MOFs. The desorption isotherm also exhibits steps at the corresponding inflection points of the adsorption isotherm, but does not trace the adsorption process. There are, therefore, marked broad hysteresis loops confirming that the adsorbed CO_2 is not immediately released on reducing the external pressure and is thus trapped within the framework. However, all of the trapped CO_2 can be released on returning to $P/P_0 = 0$. To gain more insight into this intriguing sorption system, the CO_2 sorption isotherms were measured at various temperatures (205–303 K) and up to relatively high pressure to guarantee comparable adsorption uptakes. Between 205 and 213 K, the CO_2 adsorption isotherms show the first adsorption step at a similar P/P_0 as at 195 K, but with the second and third steps merging and becoming less distinct (Supplementary Fig. S29). The corresponding desorption also gives a hysteresis loop but one that is narrower than at 195 K. In contrast, over a higher temperature range (221–303 K), all CO_2 isotherms are completely reversible without any adsorption step or hysteresis loop (Fig. 4b). Interestingly, isotherms at 195 and 221 K show a similar uptake capacity at $P/P_0 = 1.0$ despite different adsorption

isotherm profiles at lower partial pressures, indicating that CO_2 adsorption undergoes different processes at these temperatures, but reaching the same adsorbate/adsorbent system at $P/P_0 = 1.0$. Thus, importantly, the CO_2 adsorption/desorption hysteresis in NOTT-202a is highly temperature dependent.

The CO_2 isotherms can be classed into two groups: those recorded between 195 and 213 K, below the triple point of CO_2 (216.7 K); and those recorded between 221 and 303 K, above the triple point (Fig. 4c). At temperatures below the triple point, adsorption equilibria can be built up by adsorbed CO_2 molecules in a thermodynamically more ordered state than in the fluid phase at above the triple point. Interestingly, X-ray crystallographic structural studies of H_2- and CO_2-loaded porous coordination materials revealed an ordered adsorbed state for molecular H_2 and CO_2 (refs 36,37). Comparison of the two groups of isotherms clearly shows that the adsorption/desorption hysteresis is present only when the system is exposed to temperatures below the triple point (Fig. 4c). Interestingly, stepwise and hysteretic CO_2 sorption in a flexible MOF material has been reported, and corresponding adsorption steps and desorption hysteresis were also found in
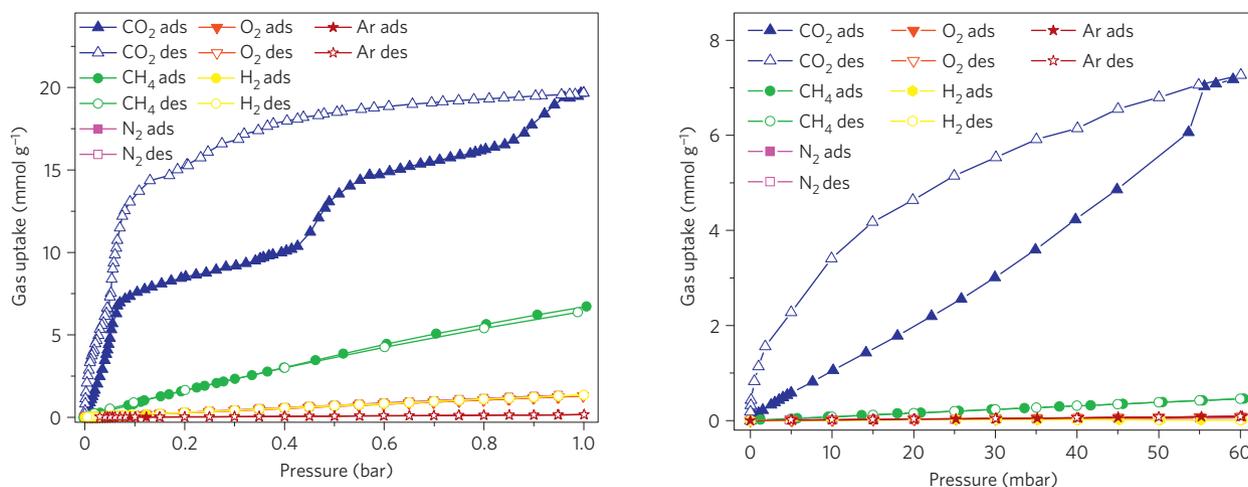
Figure 6 | Comparisons of low-pressure CO_2, CH_4, N_2, Ar, O_2 and H_2 sorption isotherms at 195 K. The CO_2 isotherms exhibit a marked hysteresis loop, whereas other gas isotherms show good reversibility and low uptake capacities. At 195 K and 60 mbar, the CO_2 uptake was found to be 17–140 times (on a molar basis) higher than uptakes of CH_4, N_2, O_2, Ar or H_2 under the same conditions. In contrast, at 273 K and 1.0 bar, the CO_2 uptake was only 3.5–22 times higher than uptakes of CH_4, N_2, O_2, Ar or H_2 under the same conditions.

N_2 and Ar isotherms at certain gating pressure[38]. However, in contrast, no apparent adsorption step or hysteresis loop was observed in the isotherms for N_2 and Ar uptake in NOTT-202a (Supplementary Fig. S22). This is consistent with the observed reversible isotherms for N_2, Ar and H_2 adsorption because the corresponding experimental temperatures are higher than their triple points (63.1 K for N_2, 83.8 K for Ar and 13.8 K for H_2), where the guest molecules are in the fluid state within the micropores. Significantly, the adsorption/desorption hysteresis in NOTT-202a is exclusively coupled with microscopic CO_2–host ordering in the micropores below the triple point (see below). This distinct process represents a new strategy to induce adsorption/desorption hysteresis that can selectively respond to a certain adsorbate by judicious choice of temperatures linked to flexibility of the porous host[18–22,39].

The values of adsorption isosteric heat Q_{st} lie in the range 20–25 kJ mol^{-1} and decrease initially from 22 kJ mol^{-1} to ~20 kJ mol^{-1} for CO_2 uptakes of 1–4 mmol g^{-1}; they then increase continuously thereafter to ~25 kJ mol^{-1} at 12 mmol g^{-1} (Fig. 4d). Q_{st} has a relatively narrow range (20–22 kJ mol^{-1}) for CO_2 uptakes up to 7 mmol g^{-1}. The adsorption entropy (ΔS) decreases continuously with increasing surface coverage up to 12 mmol g^{-1}, corresponding to an increasing structural order of the system. These results suggest that the adsorption system (CO_2–host) for the hysteretic group and non-hysteretic group of isotherms are consistent at low surface coverage, and, with increasing CO_2 loadings, the adsorption system becomes more ordered. This is driven by the adsorption enthalpy and is consistent with adsorption/desorption hysteresis observed below the triple point. Thus, NOTT-202a shows intra-pore CO_2–host ordering coupled to a broad adsorption/desorption hysteresis that is temperature dependent.

To probe and gain insight into NOTT-202a–CO_2 interactions at temperatures below and above the triple point of CO_2, *in situ* powder diffraction studies on NOTT-202a at various CO_2 adsorption/desorption loadings were carried out at 195 and 273 K. At 195 K, the powder diffraction pattern on bare material (fully degassed under vacuum) confirms that the framework remains intact after degassing; shifting and splitting of peaks were observed on loading NOTT-202a with CO_2 (Fig. 5a,c), confirming a degree of flexing of the framework on CO_2 loading. At desorption loadings of CO_2, the powder patterns show peaks shifting in the opposite direction to the adsorption branch, confirming the reversibility of

the framework phase change. Comparison of the powder patterns of bare NOTT-202a and CO_2-loaded NOTT-202a reveals that the intensity of diffraction in the latter material increases by ~15% on CO_2 inclusion (Supplementary Fig. S21). Given that there was no change in the experimental set-up of the sample or the synchrotron beam before and after CO_2 loading, the enhanced diffraction intensity confirms microscopic CO_2–host ordering below the triple point of CO_2, consistent with the measurements of adsorption entropy ΔS described above. In contrast, at 273 K, the diffraction patterns of NOTT-202a remain the same at different CO_2 adsorption/desorption loadings without any shifts in peak positions or changes in their intensities (Fig. 5b,d).

Stepwise adsorption in NOTT-202a has been simulated using a model framework in which 87.2% of the volume was occupied by doubly interpenetrated (2.0) net, 4.8% of the volume incorporating 6-Å-wide slit pores and 8.0% 10Å-wide slit pores as shown in Supplementary Fig. S55. This model framework represents the structural features observed in the 1.75 partially interpenetrated net by taking the 2.0 network and introducing linear defects (slits). The width of the slit defects was defined as the distance between opposite dangling ligands in nets B_1 and B_2 (Supplementary Fig. S56). Using this model, the experimentally observed three-step adsorption isotherm can be successfully reproduced (Supplementary Fig. S57) and explained by sequential filling of different pores within the MOF (ref. 40). Step 1 corresponds to initial filling of 2.0 net at $P \leq 0.42$ bar (Supplementary Fig. S58a,b). The pore defects are next filled with sorbate CO_2 molecules adsorbing into the narrower (6 Å wide) slit pores at higher pressures 0.42 bar $\leq P \leq 0.88$ bar (step 2) and then into the wider (10 Å wide) slit pores at $P \geq 0.88$ bar (step 3). This theoretical isotherm of course corresponds to an idealized structure containing no impurities, further defects or collapsed regions that may naturally exist in the experimental sample. Discrepancy between theory and experiment is also to be expected given the uncertainty in the magnitude of host–guest and guest–guest interactions and the overall charge distribution of the framework. Flexing of the framework on gas loading will also contribute to differences between theory and experiment.

To examine the selectivity of CO_2 capture by NOTT-202a, sorption isotherms for a range of common gas CH_4, N_2, O_2, H_2 and Ar were measured up to 1.0 bar at 195 K (below the triple point) at 273 K (above the triple point) and at 293 K (ambient temperature) (Fig. 6 and Supplementary Figs S34 and

Table 1 | CO$_2$ selectivity data from Henry's law analysis of isotherm data at 195, 273 and 293 K.

Selectivity ratio	195 K		273 K	293 K
	Adsorption	Desorption	Adsorption	Adsorption
CO$_2$/CH$_4$	23.7(7)	102(2)	2.92(14)	1.41(5)
CO$_2$/N$_2$	285(13)	1,220(51)	26.7(6)	4.25(10)
CO$_2$/O$_2$	145(5)	622(15)	27.3(7)	3.00(8)
CO$_2$/Ar	138(4)	592(14)	22.6(5)	6.51(7)
CO$_2$/H$_2$	1,867(66)	8,000(230)	>10^5	>10^5

S35). All isotherms show relatively low uptake capacities and fully reversible type-I characteristics with fast kinetics. In contrast, CO$_2$ sorption isotherms were measured up to 60 mbar at 195 K, where the first sharp rise was recorded at a significant uptake of 7.52 mmol g^{-1} (33.1 wt%). In addition, the desorption isotherm of CO$_2$ below 60 mbar shows a marked hysteresis loop and relatively slow kinetics, reflecting the strong affinity of the host for CO$_2$. Thus, the broad hysteretic CO$_2$ sorption behaviour gives rise to an effective trapping and capture mechanism for CO$_2$ from gaseous mixtures. On slowly decreasing the external pressure after adsorption at relatively high pressures, other gases with good isotherm reversibility are released, selectively leaving the CO$_2$ trapped by means of hysteresis in the framework. However, once above the triple point, the fully reversible CO$_2$ isotherms at 273 and 293 K show much lower uptake capacities of 0.17 mmol g^{-1} (0.75 wt%) at 60 mbar and 2.44 mmol g^{-1} (10.7 wt%) at 1.0 bar.

At 273 K, the selectivity ratio of CO$_2$ in NOTT-202a, obtained from Henry's law, is 2.9:1, 27:1 and 27:1 for CH$_4$, N$_2$ and O$_2$, respectively (Table 1). These values are lower than the selectivity ratio obtained at ambient temperature for ranges of other MOF/ZIF (ZIF: zeolitic imidazolate framework) and carbon molecular sieve materials that show selectivities of 10:1 for CO$_2$/CH$_4$, 81:1 for CO$_2$/N$_2$ and 50:1 for CO$_2$/O$_2$ (refs 41–43). In contrast, at 195 K, below the triple point, excellent selectivity of adsorption of CO$_2$ was observed at 24:1 for CO$_2$/CH$_4$, 285:1 for CO$_2$/N$_2$ and 145:1 for CO$_2$/O$_2$ (Table 1), higher than for other MOF/ZIF and carbon molecular sieve materials[39,41–43]. Importantly, the selectivity of trapping of CO$_2$ is enhanced (by about four times) by the hysteretic CO$_2$ desorption coupled with microscopic CO$_2$–host ordering, yielding extremely high values at 102:1 for CO$_2$/CH$_4$, 1,220:1 for CO$_2$/N$_2$ and 622:1 for CO$_2$/O$_2$. This suggests that NOTT-202a, with a gas storage capacity of up to 20 mmol g^{-1} at 1.0 bar, has the potential to selectively capture and trap CO$_2$ from gaseous mixtures with high efficiency below the triple point. Thus, the selectivity for CO$_2$ over other gases in NOTT-202a can be modulated by choice of operation temperature and enhanced by the selective hysteretic CO$_2$ desorption. This represents a new class of flexible network solids capable of efficient and effective capturing of CO$_2$.

The selective adsorption of CO$_2$ over CH$_4$, O$_2$, N$_2$ and H$_2$ has been reported for a series of interpenetrated MOF materials at 195 K based on a micropore gating effect of the kinetic diameter (3.3 Å) of CO$_2$ (refs 29,30). However, these materials all exhibit relatively low total uptake capacities (1.3–5.8 mmol g^{-1} at 1.0 bar) for CO$_2$. Interestingly, it has been reported that the hydrated form of Cr-MIL-53 shows a significantly enhanced ability to selectively capture CO$_2$ from CO$_2$/CH$_4$ mixtures with broadly hysteretic desorption of CO$_2$ coupled with a breathing transformation[15]. However, in this case higher pressures (20 bar) are required to guarantee good separations.

This work reports a unique material, NOTT-202, showing partial double interpenetration in which net *A* is fully present whereas net *B* shows an occupancy of only 0.75. This structure has been rationalized on the basis of net *B* comprising two symmetry-related components, net B_1 and net B_2, that cannot connect to one another owing to steric clashes, thus forming defects throughout the structure. NOTT-202a exhibits the highest BET surface area and CO$_2$ storage capacity for a MOF incorporating In(III). Thus, the unusual and enhanced adsorption properties of NOTT-202a for CO$_2$ are linked directly to the stepwise filling of pores and structural vacancies generated by this partially interpenetrated 1.75 defect material.

Methods

Synthesis of H$_4$L. The ligand biphenyl-3,3′,5,5′-tetra-(phenyl-4-carboxylic acid) was synthesized using a Suzuki coupling reaction. Biphenyl-3,3′,5,5′-tetrabromide (0.47 g, 1.0 mmol), 4-boronic acid phthalic acid (1.16 g, 6.0 mmol) and K$_3$PO$_4$ (1.68 g, 8.0 mmol) were mixed in 1,4-dioxane (60 ml), and the mixture was de-aerated under Ar for 20 min. [Pd(PPh$_3$)$_4$] (0.05 g, 0.022 mmol) was added to the reaction mixture with stirring and the mixture heated to 85 °C for three days under Ar. The product Et$_4$L was isolated by conventional extraction procedures. The final product H$_4$L was obtained by hydrolysis of the crude product Et$_4$L with 2 M aqueous NaOH, followed by acidification with concentrated HCl. Yield: 0.54 g, 85%. ^{1}H NMR (dimethylsulphoxide-d_6, 300 MHz), Et$_4$L: 8.20 (d, $J = 8$ Hz, 8H), 7.94 (s, 4H), 7.90 (s, 2H), 7.81 (d, $J = 8$ Hz, 8H), 4.45 (q, 8H), 1.45 (t, 12H). H$_4$L: 8.25 (d, $J = 1.5$ Hz, 8H), 8.09 (m, 14H). Elemental analyses (percentage calculated/found) for H$_4$L(C$_{40}$H$_{26}$O$_8$) : C 75.7/75.3, H: 4.13/4.17. Mass (ESI) m/z (M–H$^+$): 633.16.

Synthesis of (Me$_2$NH$_2$)$_{1.75}$[In(L)]$_{1.75}$·(DMF)$_{12}$·(H$_2$O)$_{10}$ (NOTT-202). H$_4$L (0.030 g, 0.047 mmol) and In(NO$_3$)$_3$ (0.014 g, 0.047 mmol) were mixed and dispersed in a mixture of DMF/CH$_3$CN (3.0 ml, 2:1 v/v). The resulting white slurry turned clear on addition of two drops of 6 M HNO$_3$ solution. The solution was heated to 90 °C for 1 day and the colourless crystalline product was separated by filtration, washed with DMF and dried in air. Yield: 0.05 g (70%). Elemental analysis (percentage calculated/found): for In$_{1.75}$O$_{36}$C$_{109.5}$H$_{156.5}$N$_{13.75}$ (C 53.8/53.6, H 6.46/6.57, N 7.89/7.98). Selected infrared: $\nu = 3,048$(w), 2,945(w), 2,808(w), 1,704(vs), 1,606(m), 1,587(m), 1,380(vs), 1,254(m), 1,100(m), 856(m), 781(s), 706(w), 661(m).

Crystal data for NOTT-202. [Me$_2$NH$_2$]$_{1.75}$[In(C$_{40}$H$_{22}$O$_8$)]$_{1.75}$·12(C$_3$H$_7$NO)·10H$_2$O. Colourless tabular crystal (0.10 × 0.05 × 0.04 mm). Orthorhombic, *F*222 (no. 22), $a = 16.512(7)$, $b = 25.952(11)$, $c = 30.569(12)$ Å, $V = 13,100(9)$ Å^3, $M = 2,442.42$, $T = 120(2)$ K, $Z = 4$, $D_{calc} = 1.238$ g cm^{-3}, $\mu = 0.386$ mm^{-1}, $F(000) = 5,134$. Of 11,352 reflections measured, 5,065 were unique ($R_{int} = 0.080$) and were used in all calculations. Final $R_1 = 0.0776$ [3,901 $F > 4\sigma(F)$], wR_2 [all F^2] = 0.193 with GOF = 0.99. The final difference Fourier extrema were 0.75 and −1.39 e Å^{-3}.

Crystal data for NOTT-202a. [Me$_2$NH$_2$]$_{1.75}$[In(C$_{40}$H$_{22}$O$_8$)]$_{1.75}$. Colourless tabular crystal (0.10 × 0.08 × 0.05 mm). Monoclinic, space group *C*2/*c* (no. 15), $a = 19.814(7)$, $b = 28.330(10)$, $c = 26.219(10)$ Å, $\beta = 97.87(1)°$, $V = 14,580(9)$ Å^3, $M = 1,385.11$, $T = 120(2)$ K, $Z = 4$, $D_{calc} = 0.631$ g cm^{-3}, $\mu = 0.308$ mm^{-1}, $F(000) = 2,814$. Of 31,585 reflections measured, 12,789 were unique ($R_{int} = 0.047$) and were used in all calculations. Final $R_1 = 0.0479$ [9,429 $F > 4\sigma(F)$], wR_2 [all F^2] = 0.131 with GOF = 1.00. The final difference Fourier extrema were 1.31 and −0.76 e Å^{-3}.

Crystal data for NOTT-214. [Me$_2$NH$_2$][In(C$_{40}$H$_{22}$O$_8$)]·H$_2$O. Colourless prismatic crystal (0.04 × 0.02 × 0.02 mm). Orthorhombic, space group *Pban* (no. 50), $a = 14.746(6)$, $b = 11.038(5)$, $c = 12.306(5)$ Å, $V = 2,003.2(14)$ Å^3, $M = 809.51$, $T = 90(2)$ K, $Z = 2$, $D_{calc} = 1.342$ g cm^{-3}, $\mu = 0.643$ mm^{-1}, $F(000) = 824$. Of 9,286 reflections measured, 2,133 were unique ($R_{int} = 0.029$) and were used in all calculations. Final $R_1 = 0.0587$ [1,910 $F > 4\sigma(F)$], wR_2 [all F^2] = 0.168 with GOF = 1.00. The final difference Fourier extrema were 1.06 and −0.78 e Å^{-3}. Crystallographic data have been deposited with the Cambridge Crystallographic Data Centre as supplementary publications CCDC 756304, 789578–789583 and 850840 for NOTT-202, NOTT-202a and NOTT-214, respectively.

References
1. Magudeswaran, P. N., George, S. & John, J. Reduction of global warming gas emissions from the manufacture of portland cement using high volume fly ash concrete. *Nature Environ. Pollut. Technol.* **6**, 495–497 (2007).
2. Davis, M. E. Ordered porous materials for emerging applications. *Nature* **417**, 813–821 (2002).
3. Long, J. R. & Yaghi, O. M. (eds) Special issue on metal–organic frameworks. *Chem. Soc. Rev.* **38**, 1201–1507 (2009).

4. Banerjee, R. *et al*. High-throughput synthesis of zeolitic imidazolate frameworks and application to CO_2 capture. *Science* **319**, 939–943 (2008).
5. Sumida, K. *et al*. Hydrogen and carbon dioxide capture in an iron-based sodalite-type metal–organic framework (FE-BTT) discovered via high-throughput methods. *Chem. Sci.* **1**, 184–191 (2010).
6. Millward, A. R. & Yaghi, O. M. Metal-organic frameworks with exceptionally high capacity for storage of carbon dioxide at room temperature. *J. Am. Chem. Soc.* **127**, 17998–17999 (2005).
7. Llewellyn, P. L. *et al*. High uptakes of CO_2 and CH_4 in mesoporous metal–organic frameworks MIL-100 and MIL-101. *Langmuir* **24**, 7245–7250 (2008).
8. Furukawa, H. *et al*. Ultrahigh porosity in metal–organic frameworks. *Science* **329**, 424–428 (2010).
9. Britt, R. D., Furukawa, H., Wang, B., Glover, T. G. & Yaghi, O. M. Highly efficient separation of carbon dioxide by a metal–organic framework replete with open metal sites. *Proc. Natl Acad. Sci. USA* **106**, 20637–20640 (2009).
10. Vaidhyanathan, R. *et al*. Direct observation and quantification of CO_2 binding within an amine-functionalised nanoporous solid. *Science* **330**, 650–653 (2010).
11. Demessence, A., D'Alessandro, D. M., Foo, M. L. & Long, J. R. Strong CO_2 binding in a water-stable, triazolate-bridged metal–organic framework functionalized with ethylenediamine. *J. Am. Chem. Soc.* **131**, 8784–8786 (2009).
12. Dietzel, P. D. C., Besikiotis, V. & Blom, R. Application of metal–organic frameworks with coordinatively unsaturated metal sites in storage and separation of methane and carbon dioxide. *J. Mater. Chem.* **19**, 7362–7370 (2009).
13. Dybtsev, D. N., Chun, H., Yoon, S. H., Kim, D. & Kim, K. Microporous manganese formate: A simple metal–organic porous material with high framework stability and highly selective gas sorption properties. *J. Am. Chem. Soc.* **126**, 32–33 (2004).
14. Shimomura, S. *et al*. Selective sorption of oxygen and nitric oxide by an electron-donating flexible porous coordination polymer. *Nature Chem.* **2**, 633–637 (2010).
15. Llewellyn, P. L., Bourrelly, S., Serre, C., Filinchuk, Y. & Férey, G. How hydration drastically improves adsorption selectivity for CO_2 over CH_4 in the flexible chromium terephthalate MIL-53. *Angew. Chem. Int. Ed.* **45**, 7751–7754 (2006).
16. Walton, K. S. *et al*. Understanding inflections and steps in carbon dioxide adsorption isotherms in metal–organic frameworks. *J. Am. Chem. Soc.* **130**, 406–407 (2008).
17. Thallapally, P. K. *et al*. Gas-induced transformation and expansion of a non-porous organic solid. *Nature Mater.* **7**, 146–150 (2008).
18. Férey, G. & Serre, C. Large breathing effects in three-dimensional porous hybrid matter: Facts, analyses, rules and consequences. *Chem. Soc. Rev.* **38**, 1380–1399 (2009).
19. Thallapally, P. K. *et al*. Flexible (breathing) interpenetrated metal–organic frameworks for CO_2 separation applications. *J. Am. Chem. Soc.* **130**, 16842–16843 (2008).
20. Wang, Z. & Cohen, S. M. Modulating metal–organic frameworks to breathe: A postsynthetic covalent modification approach. *J. Am. Chem. Soc.* **131**, 16675–16677 (2009).
21. Seo, J., Matsuda, R., Sakamoto, H., Bonneau, C. & Kitagawa, S. A pillared-layer coordination polymer with a rotatable pillar acting as a molecular gate for guest molecules. *J. Am. Chem. Soc.* **131**, 12792–12800 (2009).
22. Choi, H-S. & Suh, M. P. Highly selective CO_2 capture in flexible 3D coordination polymer networks. *Angew. Chem. Int. Ed.* **48**, 6865–6869 (2009).
23. Rabone, J. *et al*. An adaptable peptide-based porous material. *Science* **329**, 1053–1057 (2010).
24. Tanaka, D. *et al*. Preparation of flexible porous coordination polymer nanocrystals with accelerated guest adsorption kinetics. *Nature Chem.* **2**, 410–416 (2010).
25. Spek, A. L. Single-crystal structure validation with the program PLATON. *J. Appl. Crystallogr.* **36**, 7–13 (2003).
26. Yaghi, O. M. Metal–organic frameworks: A tale of two entanglements. *Nature Mater.* **6**, 92–93 (2007).
27. Yang, S. *et al*. Cation-induced kinetic trapping and enhanced hydrogen adsorption in a modulated anionic metal–organic framework. *Nature Chem.* **1**, 487–493 (2009).
28. Chen, B., Eddaoudi, M., Hyde, S. T., O'Keefe, M. & Yaghi, O. M. Interwoven metal–organic framework on a periodic minimal surface with extra-large pores. *Science* **291**, 1021–1023 (2001).
29. Chen, B. *et al*. Rationally designed micropores within a metal–organic framework for selective sorption of gas molecules. *Inorg. Chem.* **46**, 1233–1236 (2007).
30. Chen, B., Ma, S., Hurtado, E. J., Lobkovsky, E. B. & Zhou, H. C. A triply interpenetrated microporous metal–organic framework for selective sorption of gas molecules. *Inorg. Chem.* **14**, 8490–8492 (2007).
31. Zhang, J., Wojtas, L., Larsen, R. W., Eddaoudi, M. & Zaworotko, M. J. Temperature and concentration control over interpenetration in a metal–organic material. *J. Am. Chem. Soc.* **131**, 17040–17041 (2009).
32. Shekhah, O. *et al*. Controlling interpenetration in metal–organic frameworks by liquid-phase epitaxy. *Nature Mater.* **8**, 481–484 (2009).
33. Farha, O. K., Malliakas, C. D., Kanatzidis, M. G. & Hupp, J. T. Control over catenation in metal–organic frameworks via rational design of the organic building block. *J. Am. Chem. Soc.* **132**, 950–952 (2010).
34. Lin, X. *et al*. High capacity hydrogen adsorption in Cu(II) tetracarboxylate framework materials: The role of pore size, ligand functionalization, and exposed metal sites. *J. Am. Chem. Soc.* **131**, 2159–2171 (2009).
35. Zheng, S. *et al*. Porous indium-organic frameworks and systematization of structural building blocks. *Angew. Chem. Int. Ed.* **123**, 9020–9024 (2011).
36. Takamizawa, S. & Nakata, E. I. Direct observation of H_2 adsorbed state within a porous crystal by single crystal X-ray diffraction analysis. *Cryst. Eng. Commun.* **7**, 476–479 (2005).
37. Takamizawa, S., Nakata, E. I., Yokoyama, H., Mochizuki, K. & Mori, W. Carbon dioxide inclusion phase of a transformable 1D coordination polymer host $[Rh_2(O_2CPh)_4(pyz)]_n$. *Angew. Chem. Int. Ed.* **42**, 4331–4334 (2003).
38. Mulfort, K. L., Farha, O. K., Malliakas, C. D., Kanatzidis, M. G. & Hupp, J. T. An interpenetrated framework material with hysteretic CO_2 uptake. *Chem. Eur. J.* **16**, 276–281 (2010).
39. Horike, S., Shimomura, S. & Kitagawa, S. Soft porous crystals. *Nature Chem.* **1**, 695–704 (2009).
40. Yuan, D., Getman, R. B., Wei, Z., Snurr, R. Q. & Zhou, H-C. Stepwise adsorption in a mesoporous metal–organic framework: Experimental and computational analysis. *Chem. Commun.* **22**, 10228–10234 (2012).
41. An, J., Geib, S. J. & Rosi, N. L. High and selective CO_2 uptake in a cobalt adeninate metal–organic framework exhibiting pyrimidine- and amino-decorated pores. *J. Am. Chem. Soc.* **132**, 38–39 (2010).
42. Banerjee, R. *et al*. Control of pore size and functionality in isoreticular zeolitic imidazolate frameworks and their carbon dioxide selective capture properties. *J. Am. Chem. Soc.* **131**, 3875–3877 (2009).
43. Reid, C. R. & Thomas, K. M. Adsorption of gases on a carbon molecular sieve used for air separation: Linear adsorptives as probes for kinetic selectivity. *Langmuir* **15**, 3206–3218 (1999).

Author contributions

S.Y., X.L., K.M.T., M. Schröder: syntheses, characterization, measurements and analysis of adsorption isotherms. E.B. and M. Suyetin: grand canonical Monte Carlo modelling. S.Y., A.J.B., C.C.T. and J.E.P.: synchrotron X-ray powder data analysis. S.Y., A.J.B., W.L., D.R.A. and P.J.R.: single-crystal X-ray structural data analyses. S.Y., A.J.B., P.H., N.R.C., K.M.T. and M. Schröder: overall design, direction and supervision of project. All authors contributed to the writing of the paper.

Additional information

The authors declare no competing financial interests. Supplementary information accompanies this paper on www.nature.com/naturematerials. Reprints and permissions information is available online at www.nature.com/reprints. Correspondence and requests for materials should be addressed to S.Y. or M. Schröder.